Separation method for oxygen mass transport coefficient in two phase porous air electrodes - Transport in gas and solid polymer or liquid electrolyte phases

Final report

Proposal No. 62612-CH-II

Grant No. W911NF-12-1-0549

Tatyana V. Reshetenko (PI) and Jean St-Pierre (co-PI)

Foreword

The performance of fuel cells at high current density is limited by the transport of oxygen within the porous electrodes. A better understanding of this transport process is necessary to improve the performance as well as decrease the fuel cell size in applications with volume requirements. A novel method to determine the oxygen mass transport coefficient and its separation into gas and ionomer contributions was developed. The method is based on the use of a limiting current density distribution mathematical model and different diluent gases with varying molecular weights. A linear relationship between the inverse overall mass transport coefficient and the diluent molecular weight was revealed. Because the use of different gas diluents with different molecular weight only affect the mass transport coefficient in the gas phase, an extrapolation to a zero diluent weight gives the O_2 mass transport coefficient in the ionomer phase. The gas phase mass transport coefficient is then calculated using the additive relation between the overall mass transport coefficient and its components. The O_2 mass transport coefficient in the electrolyte phase (k_e) was found to be equal to 0.01284 m s^{-1}, while in N_2 diluent k_g is equal to 0.02727 m s^{-1}.

Demonstration of this method's validity was established by comparison with the published data and with the mass transport coefficients determined by the available traditional method involving the measurement of the overall cell limiting current at different reagent flow rates. The traditional method is not applicable at low reactant flow rates. In contrast, the novel distribution method is valid over the entire flow field length and is independent of the reactant flow rate. In addition, the current distribution requires only a single experiment to determine the overall mass transfer coefficient, whereas the traditional method requires a series of experiments.

The effect of operating temperature on the mass transport coefficient was studied. The mass transport coefficient in the gas phase was found to increase with temperature. A growth of the ionomer mass transport coefficient was observed in the temperature range of 40-60°C, and its decrease was found in the range of 70-80°C. The decrease of the ionomer mass transport coefficient at high temperatures might be related to excessive water production and its condensation which

1

leads to oxygen diffusion through the liquid phase and results in the observed temperature dependence of the coefficient.

Application of the method for characterization of membrane-electrode assembly (MEA) with different gas diffusion layers (GDL) was performed and discussed. The GDL's MPL were found to have a significant influence on the ionomer mass transport coefficient: k_e was 0.02032 m s^{-1} for a MEA with a GDL without MPL, whereas for a GDL with MPL it was 0.01465 m s^{-1}. The observed MPL impact might be attributed to the texture similarity of MPL and the catalyst layer and the same diffusion mechanism. The oxygen mass transport coefficients in nitrogen media ($k_{g,\ N2}$) were found to be similar: 0.02736 and 0.02853 m s^{-1}, respectively. This finding opens a path for further optimization of the method.

To expand the scope of the activity, additional experiments were performed beyond the initial mandate. O$_2$ concentration was chosen as one of the important operating parameter, and its impact on mass transport coefficient was also studied. The results indicated that a high oxygen concentration (7-10%) is not favorable for the determination of the mass transport coefficient because the inlet segments did not reach the limiting current. Additionally, it should be noted that the mass transport coefficient in the ionomer phase (k_e) appears to depend on the O$_2$ concentration in the gas stream. Application of the method for MEA characterization is very significant for fuel cell development, and the method was used for studying the effects of cathode Pt loading. In spite of the fact that cathode Pt loading and ECA were increased by factor of 2, the variation in the ionomer mass transport coefficients is not so significant: k_e amounted to 0.01284 m s^{-1} for a MEA with low Pt loading, whereas an MEA with increased loading k_e was 0.01465 m s^{-1} due to the possible difference in ionomer coating of the electrode layers for samples from different batches. However, the oxygen mass transport coefficient in nitrogen media ($k_{g,\ N2}$) was found to be very similar: 0.02727 and 0.02853 m s^{-1}, respectively.

A series of recommendations for future work is also proposed. These recommendations include activities for both method validation and method development.

Table of contents

1. List of appendixes, illustrations and tables

1.1. List of figures

1.2. List of tables

2. Statement of the problem studied

Proton exchange membrane fuel cells (PEMFCs) are the most promising candidate systems for alternative electricity generation. To meet the power density, reliability, and cost requirements that enable the mass production of fuel cells, increased power output as well as cost reduction remain the most important obstacles. To increase the power density, a fuel cell should operate at high current, where its performance is limited by the finite transport rates of the reactants and products within the gas diffusion electrode (GDE), consisting of the gas diffusion layer (GDL) and the catalyst layer. Moreover, this issue is a significant concern for a cathode because air, which is used as oxidant, is dilute and contains only 21% of oxygen. Transport limitations hamper the flow of oxygen at the cathode electrode, causing voltage losses by reducing its concentration at a catalyst surface. Additionally, transport limitations impede the flow of product water out of the electrode, keeping the membrane humidified, but in extreme cases resulting in GDE liquid water blockages. Gas transport losses depend on cell geometry, flow field design, GDE textural properties and the fuel cell operating conditions. A better understanding of this particular limitation is necessary to increase the performance and decrease the fuel cell size in applications with power system volume requirements, such as material handling, ground support equipment and unmanned vehicles [1]. At the microscopic level, reagent transport from the flow field channels to the catalyst occurs by both diffusion and convection in the gas phase, and by diffusion in the ionomer phase. Therefore, the separation of the overall mass transport coefficient into gas and ionomer phase contributions is desirable to clarify the transport mechanism and identify the rate determining step for MEA optimization.

The limiting current is the maximum current that can be obtained from a cell as the reagent concentration at the electrode surface approaches zero [2]. The limiting current characterizing the polarization curve asymptotic behavior at low cell voltage is an important membrane/electrode assembly (MEA) and GDE mass transfer characteristic. The limiting current can be used as a tool to study mass transport phenomena in PEMFC because it can provide experimental data for the investigation of correlation between the GDE structure and the fuel cell performance [3-11].

Williams *et al*. [3] investigated the factors limiting oxygen transport in the cathode GDE and found a linear relationship for the GDL permeability vs. the limiting current. Kocha [4] used limiting current measurements to separate different forms of gas diffusion in the GDE: bulk, Knudsen, and diffusion in thin ionomer films. If the gas density is low or if the pore size is small, gas molecules collide with the pore wall more frequently than with each other, a phenomenon known as Knudsen diffusion. Bulk diffusion occurs when the conditions are reversed. It should be noted that Knudsen diffusion and thin film diffusion processes are independent of the diluent concentration.

Beuscher [5] separated the mass transport parameters of the electrode and the GDL. The GDL was demonstrated to account for 26% of the total mass transport resistance, while the catalyst layer accounts for 18%. Thus, gas diffusion through the flow channel, GDL, and catalyst layer accounts for less than half of the measured mass transport resistance (~44%). Knudsen diffusion and diffusion through the ionomer and water films accounts for over half of the total resistance (~56%).

Baker *et al.* [6-8] separated the transport resistance into a pressure-dependent component (intermolecular gas diffusion) and a pressure-independent component (Knudsen diffusion or transport through ionomer/liquid water layers). The authors distinguished conditions in which water started to condense in the fuel cell and measured the impact of such conditions on the oxygen transport resistance.

Stumper *et al.* [9] developed a novel method to determine the MEA resistance and the electrode diffusion coefficient for PEMFCs under in situ conditions based on the galvanostatic discharge of a cell with an interrupted reactant supply. The results indicated that oxygen diffusion in the active layer in the electrode, where Knudsen diffusion dominates due to the small pore size, is most likely mass transport limited.

St-Pierre *et al.* [10, 11] suggested a new method using local limiting currents to determine the overall hydrogen and oxygen mass transport coefficient and its components: gas phase diffusion within the GDE and solid phase diffusion through the ionomer covering a catalyst. At the limiting current, a large gradient in reactant concentrations exist along the flow field channel. Under such operating conditions, the overall mass transfer coefficient is accurately determined by current distribution measurements. Similar measurements are repeated using other gas diluents of different molecular masses. An extrapolation of the overall mass transport coefficient curve to a diluent of zero molecular mass leads to the ionomer phase mass transfer coefficient. The subsequent use of the additive relationship between the overall, ionomer phase and gas phase mass transfer coefficients leads to the gas phase mass transfer coefficient. This new method supplements the prior efforts [5-9].

A segmented fuel cell system allowing the in situ measurement of the current distribution is the ideal tool to study local limiting currents. Such a system was developed by the Hawaii Natural Energy Institute (HNEI) [12] and represents an improvement over prior work by Cleghorn et al. [13], Ballard Power Systems Inc. [14], the German Aerospace Centre [15], and Los Alamos National Laboratory (LANL) [16]. HNEI's segmented cell system was partially based on the LANL design using closed loop Hall sensors and an improved data acquisition system allowing simultaneous, rather than sequential, measurements of the spatially variable electrochemical impedance spectra, cyclic voltammograms, and linear sweep voltammograms.

This report presents the demonstration of the newly proposed mass transfer separation method [10, 11], its validation, and application. The project includes the following objectives:

- Develop a method for determining the gas and solid polymer or the liquid electrolyte phase mass transport coefficients applicable to the air electrode, including an improved empirical correlation relating the overall oxygen mass transport coefficient to the gas diluent molecular weight.
- Obtain data with a segmented cell for the validation of the non-uniform current density distribution mathematical model.
- Investigate the impact of the selected operating conditions on the gas and solid polymer or liquid electrolyte phase mass transport coefficients. Temperature was the operating condition considered because of its large effect on the transport parameters and the wide operating temperature range requirement for applications.
- Apply the method to the study of the impact of a change in the GDL structural properties (use of different GDLs) on the gas phase mass transport coefficient to demonstrate the sensitivity of the mass transport coefficient determination method.

To expand the scope of the activity, additional experiments were performed beyond the initial aims. The O_2 concentration was chosen as one of the important operating parameters, and its impact on the mass transfer coefficient was also studied. An application of the method for MEA characterization is very significant for fuel cell development, and the method was used for studying the effects of cathode Pt loading.

3. Experimental

All experiments were conducted using Hawaii Natural Energy Institute's (HNEI) segmented cell system. This diagnostic tool enables the collection of spatially distributed information during a standard fuel cell experiment [12]. The segmented cell is operated as a single cell fuel cell using a Grandalytics test station. The current and power limitations were 240 A and 1.2 kW, respectively. The segmented cell system includes cell hardware and a data acquisition system composed of a custom built current transducer system and a National Instrument PXI data acquisition instrument (Fig. 1 a). A custom LabView program controls the National Instrument PXI. For current sensing, a closed loop Hall sensor device from Honeywell, Model CSNN191, was used. Segment currents of up to $2\,A\,cm^{-2}$ are measured in the high current mode. The maximum current density is lowered to $50\,mA\,cm^{-2}$ in the low current mode, which is typically used for spatially distributed electrochemical diagnostics: cyclic voltammetry (CV), linear sweep voltammetry (LSV) and electrochemical impedance spectroscopy (EIS).

The segmented cell hardware was based on a HNEI 100-cm^2 cell design. The hardware contains a segmented flow field, which consists of ten cell segments forming a continuous path along ten parallel serpentine channels. Each segment has an area of 7.6 cm^2 and has its own distinct current collector and GDL (Fig. 1 b). The segmented cell hardware is applicable to either the anode or the cathode.
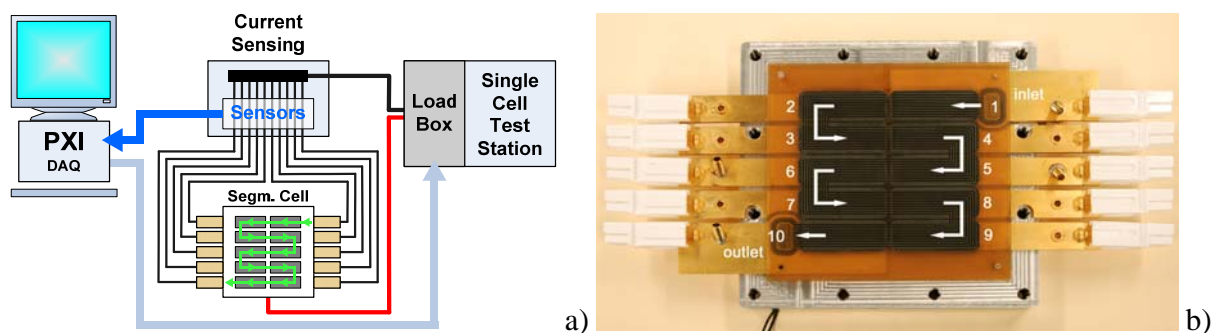
Fig. 1. Segmented cell measurement setup (a); segmented hardware and current collector plates (b).

A 100-cm^2 Gore catalyst coated membrane (CCM) with a single anode GDL and 10 cathode GDLs of reduced size to cover each segment were used. The electrodes were made of Pt/C catalyst coated on a Gore membrane (18 μm) with a loading of 0.1 and 0.2 mg Pt cm^{-2} on the anode and cathode, respectively. A standard GDL material was 25BC by Sigracet. Teflon gaskets were applied for the anode and cathode. Additionally, MEAs with 0.1/0.4 mg Pt cm^{-2} and 25BA by Sigracet were used. Table 1 presents details of the MEAs under the study. The thicknesses of 25BC and 25BA are 235 and 185 µm, respectively. The gasket materials were chosen to maintain the close compression ratio for all the MEA samples in the range from 35% (MEA1) to 38% (MEA2, MEA3).

Table 1. Parameters of the MEAs used in the study.

Sample	An/Ca Pt loading [mg$_{Pt}$ cm^{-2}]	Thickness of the electrodes and membrane [µm]	Thickness of the Kapton and membrane [µm]	An/Ca GDL	An/Ca gasket thickness [µm]
MEA1	0.1/0.2	36	88	25BC/25BC	125/125
MEA2	0.1/0.4	45	85	25BC/25BC	125/125
MEA3	0.1/0.4	45	85	25BC/25BA	125/100

Limiting current measurements were performed at 60°C. The anode/cathode operating parameters were: H$_2$/diluents + 5% vol. O$_2$, 48.3/48.3 kPa$_g$ back pressure, and 100/100% relative humidity. We used as diluents the following: He, Ne, N$_2$, Ar, CO$_2$, Kr, CF$_4$, SF$_6$, and C$_3$F$_8$. Polarization (VI) curves were measured under potentiostatic control and with fixed reactant flow rates. For some experiments, the cell temperature was varied from 40 to 80°C, and the oxygen concentration ranged from 5 to 10% vol.

The segmented cell was assembled, conditioned and tested with a set of beginning of test diagnostics before the limiting current tests were completed. Experiments were performed with the H$_2$/air and H$_2$/He+O$_2$ gas configuration with 21 vol.% O$_2$ and with a H$_2$/O$_2$ configuration. To maintain a constant water transport in the cell for any given total cell current density, the flow rates of H$_2$/He+O$_2$ and H$_2$/O$_2$ were identical to those used during the H$_2$/air operation with stoichiometry of 2. Consequently, the stoichiometry of He+O$_2$ remained 2, whereas that of O$_2$ increased to 9.5.

The three different VI curves were used to quantify the segment overpotential [12, 17]. The activation overpotential η_{act} was calculated by subtracting the ohmic loss-corrected H_2/O_2 polarization curve from the theoretical open circuit voltage of 1.23 V. The ohmic overpotential η_{Ohm} was calculated by multiplying the high-frequency resistance (HFR) with the respective current density. The $H_2/He+O_2$ data was subtracted from the H_2/O_2 data, yielding the permeability overpotential $\eta_{MT,\ perm}$; the diffusion overpotential $\eta_{MT,\ dif}$ was obtained by subtracting the H_2/air values from the $H_2/He+O_2$ values.

These experiments were combined with EIS to determine the cell and segment resistances and to obtain the electrochemical impedance spectra for all ten segments at each current density. The selected frequency range for the EIS experiments was 0.1 Hz to 10 kHz, and the amplitude of the sinusoidal total cell current signal perturbation was 2 A, resulting in a cell voltage response below 10 mV. The high-frequency resistance (HFR) was determined from the x-axis intercept of the EIS at high frequencies (Nyquist plot).

CV experiments were conducted to determine the ECA using a Parstat 2273 potentiostat/galvanostat from EG&G Instruments Corp. CV experiments were performed at a cell temperature of 35°C with a scan rate of 20 mV s^{-1} while supplying 100% humidified hydrogen and 100% humidified nitrogen to the reference (counter) electrode and the working electrode, respectively, at a flow rate of 750 ml min^{-1}. For each measurement, cycles were repeated three times with potentials from -0.015 to 1.1 V vs. the hydrogen reference electrode (HRE). The hydrogen desorption peak area of the third cycle was used to determine the ECA. Hydrogen crossover experiments were performed at identical conditions as the ECA experiments using a single potential sweep from 0.1 to 0.4 V vs. the HRE at a scan rate of 0.1 mV s^{-1}.

4. Summary of the most important results

4.1. <u>Mathematical model</u>

Fuel cell reactant transport from the flow field channels to the catalyst occurs by both diffusion and convection in the gas phase, and by diffusion in the ionomer phase. At low cell voltages, or equally at large current densities, the performance is controlled by all these transport processes. Under these operating conditions, the current density approaches a limit i_l (A m^{-2}) described with an overall mass transport coefficient k (m s^{-1}):

$$i_l = nFkc_c \tag{1}$$

where n is the number of electrons exchanged in the electrochemical reaction, F is the Faraday constant (96500 C mol^{-1}), and c_c is the local dry reactant concentration in the flow field channel (mol m^{-3}). Eq. (1) is more general than the equivalent equation derived using Fick's first law because convection is taken into account in addition to diffusion:

$$i_l = nFD\frac{dc}{dx} \approx nFD\frac{c_c - c_i}{\delta} = nFD\frac{c_c - 0}{\delta} = \frac{nFDc_c}{\delta} \tag{2}$$

where D is the reactant diffusion coefficient ($m^2\ s^{-1}$), c is the reactant concentration (mol m^{-3}), x is the Cartesian coordinate perpendicular to the MEA plane, c_i is the reactant concentration at the catalyst/ionomer interface (mol m^{-3}), and δ is the Nernst boundary layer thickness (m). The ratio D/δ is commonly referred to as the mass transfer coefficient k, and its inverse as the mass transfer resistance, R.

$$k = \frac{D}{\delta}, \quad R = \frac{1}{k} \tag{3}$$

It is emphasized that at the limiting current density, the reactant flux through the GDE is not negligible compared to the reactant flux along the flow field channel. As a result, the reactant concentration is not uniform along the flow field channel, and thus, Eq. (1) is only locally valid. For the case of a dilute reactant stream, the use of a local mass balance leads to the following current density distribution expression [11]:

$$i_l(\hat{y}) = \frac{nFkp_r f_r}{RT}e^{\frac{-nFkp_r\hat{y}}{RTi_e f}} \tag{4}$$

where $\hat{y}$ is the dimensionless position along the flow field length, p_r is the dry inlet reactant stream pressure (Pa), f_r is the reactant fraction in the dry inlet reactant stream, R is the ideal gas constant (8.3143 J mol^{-1} K^{-1}), T is the temperature (K), i_e is the inlet reactant flow rate equivalent current density (A m^{-2}) and f is the inert gas to reactant fraction in the dry inlet reactant stream. The corresponding average limiting current density i_{ave} (A m^{-2}) is [11]:

$$i_{ave} = i_e\left(1 - e^{\frac{-nFkp_r}{RTi_e f}}\right), \quad \ln\left(1 - \frac{i_{ave}}{i_e}\right) = -\frac{nFkp_r}{RT} \cdot \frac{1}{i_e f} \tag{5}$$

Determination of the mass transport coefficient was primarily accomplished with Eq. (5) or an equivalent by varying the reactant flow rate (product $i_e f$) and measuring i_{ave} [4-6, 10]. The inlet reactant flow rate equivalent current density can be expressed as:

$$i_e = \frac{nFV_{O_2}}{AV_m} \tag{6}$$

where V_{O2} is oxygen flow rate (cm^3 s^{-1}), A is the active area of the MEA (cm^2), and V_m is molar volume (22414 cm^3 mol^{-1}). The accuracy of the mass transport coefficient determination is expected to improve using local (Eq. 4) rather than average (Eq. 5) current density values, partly because a single experiment is needed instead of a series (several reactant flow rate values).

The overall mass transport coefficient is a series combination of the mass transport resistances in the gas (k_g (m s^{-1})) and ionomer electrolyte (k_e (m s^{-1})) phases, which is represented as [18]:

$$\frac{1}{k} = \frac{1}{k_g} + \frac{1}{k_e} \tag{7}$$

$$k_g = \frac{k \cdot k_e}{k_e - k} \tag{8}$$

Eq. (7) implies that different gas diluents only affect k_g [11]. The gas diluent would not have any effect if the transport were solely controlled by the ionomer phase. As a result, it is possible to separate gas and ionomer phase mass transport contributions because at the limit of a zero gas diluent molecular weight, the overall mass transport coefficient k corresponds to the ionomer mass transport coefficient k_e. In a second step, the k_g value is calculated using Eq. (8) with the extrapolated k_e value and the measured k value.

4.2. Model validation

MEA1 was used for model validation and studies the effects of O_2 concentration and temperature on the mass transport coefficient. Fig. 2 a) presents the polarization curves for the entire cell measured at different H_2/5%O_2+He flow rates. The cell reached the limiting current at all operating conditions. The obtained values of the limiting currents (i_{ave}) were applied for Eq. (5) to determine the mass transport coefficient by creating plot $\ln\left(1 - \frac{i_{ave}}{i_e}\right)$ vs $\frac{1}{i_e f}$ (Fig. 2 b). It is possible to distinguish two groups of the data in Fig. 2 b): measurements at low and high oxygen flow rates. At low oxygen flow rates, the dependence between $\ln\left(1 - \frac{i_{ave}}{i_e}\right)$ and $\frac{1}{i_e f}$ is not linear, and it was not possible to use these points for a linear fitting. For extracting the mass transport coefficient, only the average limiting currents recorded at high oxygen flow rates (76-139 cm^3 min^{-1}) were used, and k_{ave} was found to be 0.01117 m s^{-1}. The same procedure was performed for several diluents: Ne, N_2, Ar, and CO_2. Fig. 2 c) shows the linear fits between $\ln\left(1 - \frac{i_{ave}}{i_e}\right)$ and $\frac{1}{i_e f}$ for these mixtures, and the extracted mass transport coefficient values (k_{ave}) are presented in Table 2.
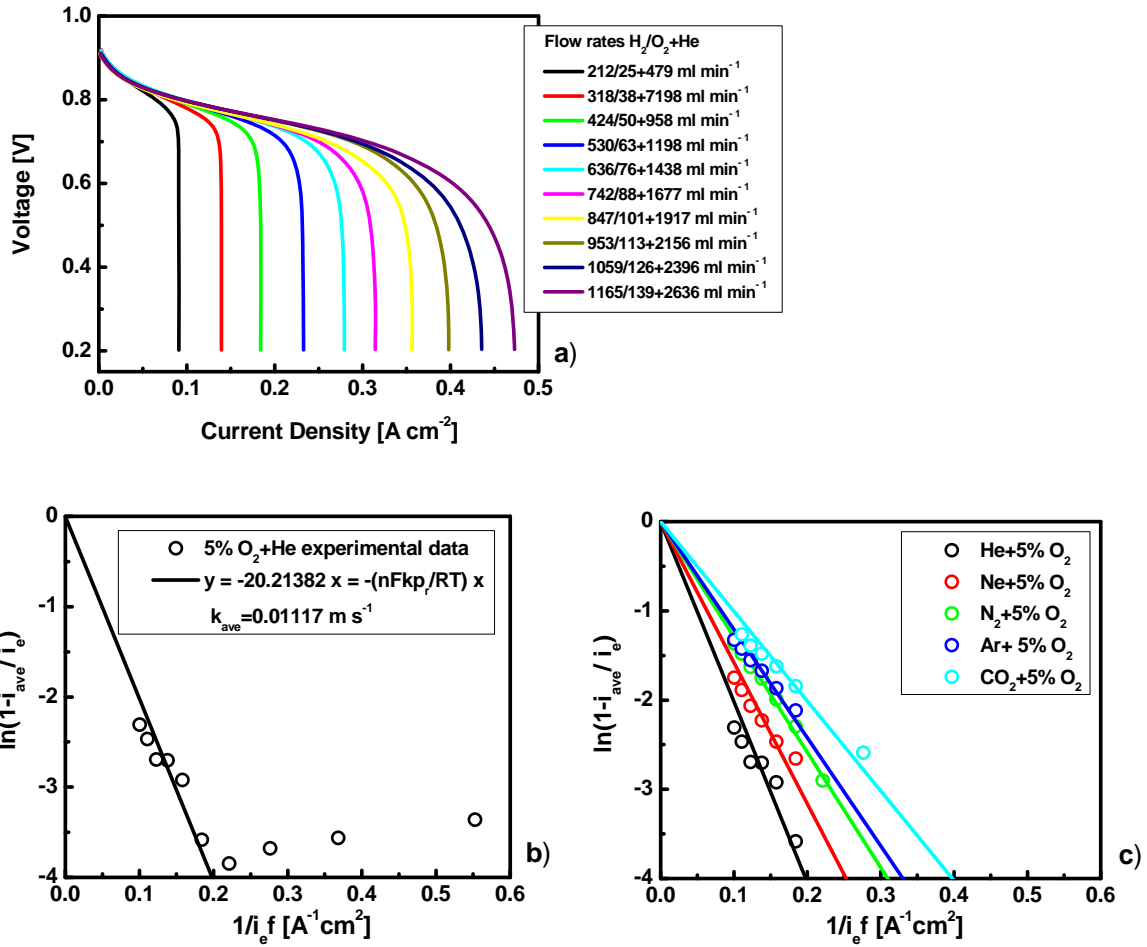
Fig. 2. Average VI curves recorded for sample 1, anode/cathode: $H_2/5\%O_2+He$, 100/100% RH, 48.3/48.3 kPa_g, and 60ºC (a); dilute reactant stream average limiting current density model (Eq. 5) validation for He (b); validation of the average limiting current density model for He, Ne, N_2, Ar, and CO_2 (c).

Fig. 3 a) and c) present the potentiostatic polarization curves (H_2/O_2+He or N_2) for the ten individual segments and the cell. All of the segments as well as the cell approach a limiting current at low cell voltages. The polarization curves qualitatively behave as expected from Eq. (4), with a decrease of the limiting current from segment 1 to 10. The change in the polarization curvature for the higher segments at an approximate cell voltage of 0.7 V (two values of cell voltage for a given current density) was observed. The same behavior was previously described for a fuel cell operated under air starvation [19].

14
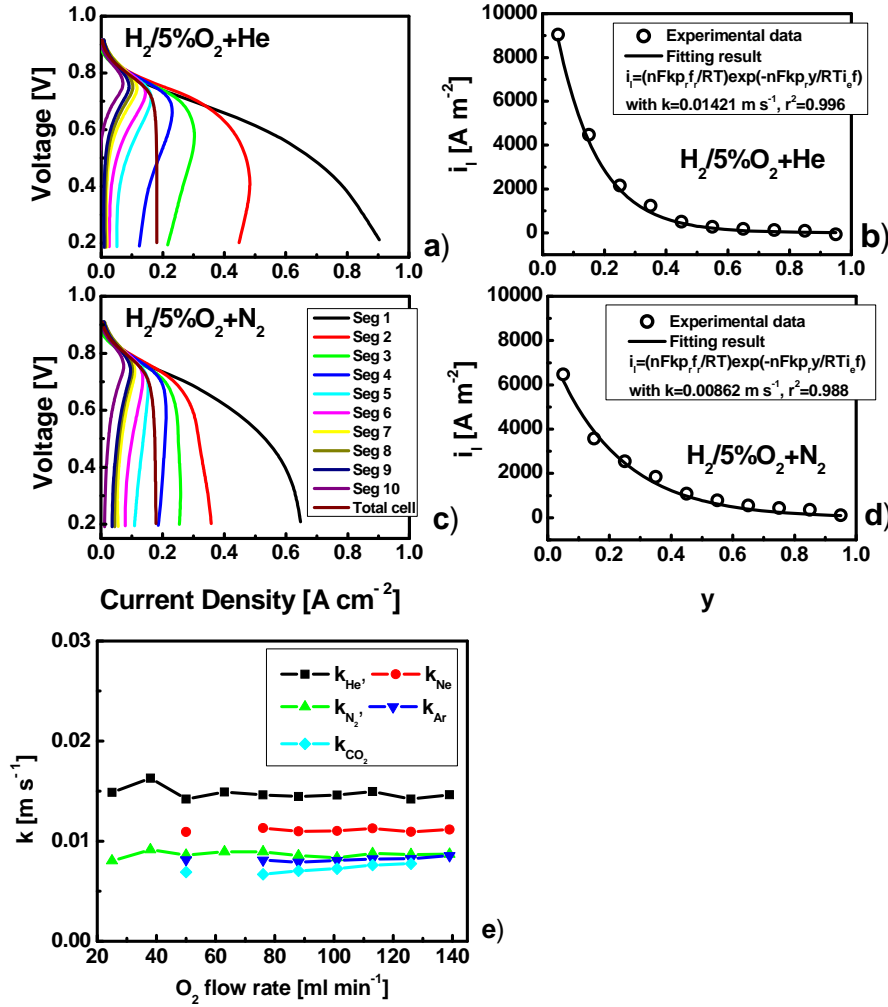
Fig. 3. Individual segments 1-10 and the overall polarization curves at different oxygen diluents: He (a), N_2 (c). Anode/cathode: H_2/5%O_2+He (or N_2), 424/50+958 cm³ min⁻¹ 100/100% RH, 48.3/48.3 kPa$_g$, and 60°C. Local limiting current model validation: He (b), N_2 (d). Dependence of the mass transport coefficient as a function of the O_2 flow rate at a constant O_2 fraction in the cathode gas stream (5%).

The inlet reactant flow rate equivalent current density i_e must be calculated to estimate the mass transport coefficient. Using Eq. (6), i_e equals to 1888.3 A m⁻², which is very close to the measured value of the overall limiting current i_l (Table 2). For our further calculations, we assumed that the oxygen stoichiometry is ~1 and $i_e=i_l$ because the outlet current density is much smaller than the inlet current density by approximately 2 orders of magnitude. The mass transfer coefficient k, the only unknown parameter in Eq. (4), was obtained by least square fitting, as shown in Figs. 3 b) and d).

Table 2 presents the oxygen mass transport coefficients k obtained by the local limiting current model according to Eq. (4). It is possible to compare two approaches to determine the coefficient: the average and the local limiting current density methods for several diluents (He, Ne, N_2, Ar, CO_2). A comparison indicates a difference between the values of k_{ave} and k. It should be noted that Eq. 5 is not applicable for a large range of flow rates. For example, Eq. 5 does not work for low reagents flow rates, as seen from Fig. 2 b). Such a phenomenon is attributed to the fact that the term i_{ave}/i_e in Eq. 5 is close to 1, which creates a larger error at the above mentioned operating conditions. This fact explains the lower values of k_{ave} extracted using Eq. 5 in comparison with k obtained by Eq. 4. Additionally, Eq. 4 provides reproducible results for a wide range of reagents flow rates, and the mass transport coefficients do not depend on this parameter (Fig. 3 e). Thus, the accuracy of the mass transport coefficient determination is improved using local (Eq. 4) rather than average (Eq. 5) current density values. Also, the local limiting current method is convenient because only a single experiment is required instead of a series of experiments (several reactant flow rate values).

Table 2. Oxygen mass transport coefficients calculated using the average limiting current density (Eq. 5, k_{ave}) and the local limiting current density (Eq. 4, k). $\bar{k} \pm \Delta k$ represents the mean value of the mass transport coefficient and its deviation obtained by Eq. (4), i_l denotes the measured cell limiting current, which was used as the average inlet reactant flow rate equivalent current density, i_e.

Diluent	M [g mol^{-1}]	k_{ave} [m s^{-1}]	k [m s^{-1}]	i_l [A m^{-2}]	$\bar{k} \pm \Delta k$ [m s^{-1}]
He	4	0.01117	0.01421	1803.5	0.0145±0.0003
Ne	20	0.00874	0.01091	1841.3	0.01095±0.00004
N_2	28	0.00715	0.00862	1780.2	0.00873±0.0003
Ar	40	0.00696	0.00813	1799.9	0.0083±0.0003
CO_2	44	0.00556	0.0069	1746.8	0.00713±0.0003
Kr	84		0.00688	1815.2	0.00688±0.0003
CF_4	88		0.00493	1687.0	0.0054±0.0005
SF_6	146		0.00397	1411.2[a)]	0.0047±0.0008
C_3F_8	188		0.00315	822.4[a)]	0.00365±0.0005

[a)] – the overall limiting current is lower than in previous cases due to the lower oxygen flow rate. The standard conditions were anode/cathode: H_2/5%O_2+diluent, 424/50+958 cm^3 min^{-1} 100/100% RH, 48.3/48.3 kPa$_g$, and 60ºC. For SF_6, the flow rates were H_2=372, O_2=44, SF_6=839 cm^3 min^{-1}. For the C_3F_8 tests, the flow rates were H_2=212, O_2=25, C_3F_8=479 cm^3 min^{-1}.

The oxygen diffusion coefficients reported in the literature are presented in Table 3. The obtained experimental values determined by the local limiting current model (Table 2) are the same order of magnitude as those which were determined using other methods. Baker found an increase of transport resistance (inverse value of the mass transport coefficient) with limiting current, due to the excess of water production and condensation [6-8].

Table 3. Oxygen mass transport coefficients previously reported in the literature.

Reference	$k_{(O2\ in\ N2)}$ [m s^{-1}]	$k_{(O2\ in\ He)}$ [m s^{-1}]	Temperature [°C]
U. Bescher [5]	0.00969	0.01379	70
J. Stumper [9]	0.00244		75
P. Berg [20]	0.00288	0.00327	80
D.R. Baker [6]	0.01111		80
D.R. Baker [8]	0.00357-0.00667		70

The impact of oxygen diluent on fuel cell performance was studied previously; however, the experiments were limited only by He, N$_2$, and Ar [4, 5, 20, 21]. It was established that mass transfer limitations are less when using He rather than Ar or N$_2$, due to the different O$_2$ diffusion rates. In the present work, a wide variety of diluents were used: He, Ne, N$_2$, Ar, CO$_2$, Kr, CF$_4$, SF$_6$, and C$_3$F$_8$. The effect of the diluent molecular weight on the overall oxygen mass transport coefficient is presented in Fig. 4, which shows a strong correlation between *1/k* and the diluent molecular weight. Such an observation is expected because the oxygen mass transport coefficient is proportional to diffusion coefficient (Eq. 2).
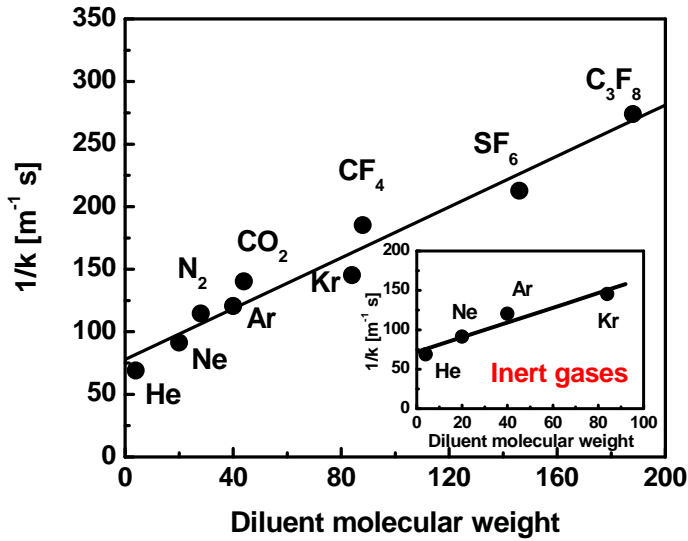
Fig. 4. Effect of the diluent molecular weight on the overall oxygen mass transport coefficient.

The bulk mass diffusivity D_{AB} for binary mixtures of nonpolar gases can be predicted using the Chapman-Enskog theory [22]. The mutual diffusion coefficient, in units of cm^2/s is defined as

$$D_{AB} = 0.0018583 \sqrt{T^3 \left(\frac{1}{M_A} + \frac{1}{M_B} \right)} \frac{1}{p\sigma_{AB}\Omega_{D,AB}} \qquad (9)$$

$$\sigma_{AB} = \frac{1}{2}(\sigma_A + \sigma_B) \qquad (10)$$

17

where T is temperature of the gas in units of Kelvin; M_A and M_B are molecular weights of species A and B, respectively; p is the total pressure of the binary mixture in units of atmospheres; σ_{AB} is the Lennard-Jones force constant for the gas mixture, which denotes the finite distance at which the inter-particle potential is zero (Å), defined by Eq. (10); and $\Omega_{D,\ AB}$ is the collision integral defined by

$$\Omega_{D,AB} = \frac{1.06036}{(T^*)^{0.15610}} + \frac{0.19300}{\exp(0.47635 \cdot T^*)} + \frac{1.03587}{\exp(1.52996 \cdot T^*)} + \frac{1.76474}{\exp(3.89411 \cdot T^*)} \quad (11)$$

where T^* is dimensionless temperature:

$$T^* = \frac{kT}{\varepsilon_{AB}} \quad (12)$$

where k is the Boltzmann gas constant, and the ratio $\dfrac{\varepsilon_{AB}}{k}$ can be estimated as

$$\frac{\varepsilon_{AB}}{k} = \left(\frac{\varepsilon_A}{k} \cdot \frac{\varepsilon_B}{k} \right)^{\!1/2} \quad (13)$$

The parameters σ_{AB} and ε_{AB} are those appearing in the Lennard-Jones potential between one molecule of A and one of B:

$$\varphi_{AB}(r) = 4\varepsilon_{AB} \left[\left(\frac{\sigma_{AB}}{r} \right)^{12} - \left(\frac{\sigma_{AB}}{r} \right)^{6} \right] \quad (14)$$

The values of σ and $\dfrac{\varepsilon}{k}$ are tabulated for most naturally occurring gases [22], and it is possible to estimate the binary gaseous diffusion coefficient. Eq. (9) indicates that the diffusion depends on the molecular weights of the gases and the so-called effective molecular diameter (σ). Table 4 presents the experimental and calculated values of the binary bulk diffusion coefficients relevant to the present study.

Note that Knudsen diffusion, which is observed when the pore size decreases, occurs when molecules collide more often with the pore walls than with each other. In this case, the mean free path of the molecule is on the same order as the diameter of the pore. Using the kinetic theory of gases to express the mean free path of the molecule, the Knudsen diffusion coefficient is given by

$$D_{K_A} = \frac{d}{3} \left(\frac{8RT}{\pi M_A} \right)^{\!1/2} \quad (15)$$

where d is the pore diameter and M_A is the molecular weight of species A [23]. Knudsen diffusion is dominant for pores that range in diameter between 2 nm and 50 nm.

Table 4. Experimental and theoretical values for the bulk binary diffusion coefficient.

Mixture A-B	Experimental data			M_B [g mol⁻¹]	σ_B [Å]	ε_B/k [K]	Ref.	Theoretical data	
	T [°C]	D [cm² s⁻¹]	Ref.					T [°C]	D [cm² s⁻¹]
O_2-O_2	0	0.187	[24]	32	3.433	113	[22]	0	0.176
	20	0.213	[25]					20	0.199
	25	0.232	[24]					25	0.206
	60	0.272	[25]					60	0.251
	80	0.301	[25]					80	0.279
O_2-He	20	0.729	[26]	4.003	2.576	10.2	[22]	20	0.720
	50	0.809	[27]					50	0.847
	60	0.889	[27]					60	0.891
	100	1.092	[26]					100	1.076
O_2-Ne				20.183	2.789	35.7	[22]	20	0.319
								60	0.397
O_2-N_2	20	0.202	[25]	28.01	3.667	99.8	[22]	20	0.197
	60	0.274	[28]					60	0.247
	100	0.307	[26]					100	0.301
O_2-Ar	20	0.187	[26]	39.948	3.432	122.4	[22]	20	0.187
	60	0.239	[29]					60	0.236
	100	0.285	[26]					100	0.288
O_2-CO_2	20	0.160	[25,26]	44.01	3.996	190.0	[22]	20	0.146
	60	0.193	[28]					60	0.185
	100	0.248	[26]					100	0.227
O_2-Kr				83.8	3.675	170.0	[22]	20	0.145
								60	0.183
O_2-CF_4				88.003	4.7	152.5	[30]	20	0.112
								60	0.141
O_2-SF_6	14	0.0651	[25]						
	20	0.097	[26]						
	100	0.154	[26]						

Dependences between the binary bulk diffusion coefficient and the mass transport coefficient vs. $\left(\frac{1}{M_{O_2}}+\frac{1}{M_{Diluent}}\right)^{1/2}$ are presented in Fig. 5 a). A strong linear correlation between the diffusion

coefficient, $D_{O2\text{-}Diluent}$, and $\left(\frac{1}{M_{O_2}}+\frac{1}{M_{Diluent}}\right)^{1/2}$ was observed, which is expected from Eq. (9).

Moreover, a linear correlation was also found for the mass transport coefficient, except for one point corresponding to He. Such behavior might be attributed to the fact that oxygen transport occurs not only in gaseous phase but also by Knudsen diffusion and through ionomer and water films, with the contribution of the latter as likely being more significant. This is especially true because He facilitates transport in the gas phase, which results in the lack of any dependence

between k_{He} and $\left(\frac{1}{M_{O_2}}+\frac{1}{M_{Diluent}}\right)^{1/2}$. Based on the data, it is possible to assume that bulk diffusion

starts to significantly influence the diffusion processes in GDE in the case of diluents with high molecular weight.

In addition, the impact of the effective molecular diameter (σ) on the mass transport coefficient and the diffusion coefficient is very pronounced for the following diluents: N_2, Ar, CO_2, Kr, CF_4 (Fig. 5 b). For example, Ar and CO_2 have close values of molecular weights (39.948 vs. 44.01 g mol^{-1}); however, the effective molecular diameters are 3.432 and 3.996 Å, respectively. These results lead to significant distinctions in the oxygen mass transport coefficient (0.0083 and 0.00713 m s^{-1} for Ar and CO_2, respectively) and the diffusion coefficient as well (Table 4). Moreover, Fig. 5 c) presents the dependence between the mass transport coefficient/diffusion coefficient vs. $\sqrt{\left(\frac{1}{M_A}+\frac{1}{M_B}\right)\frac{1}{\sigma_{AB}\Omega_{D,AB}}}$, where a linear relationship is also found.
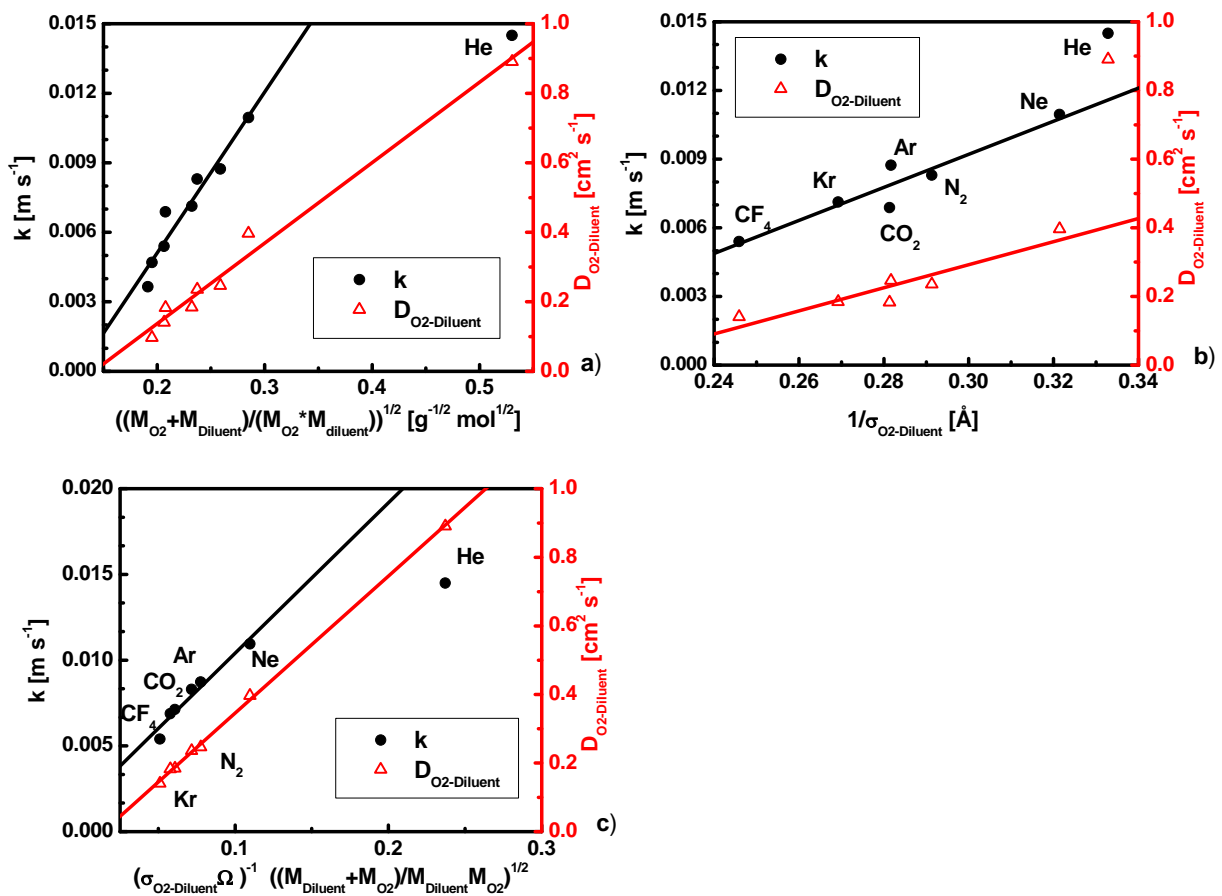
Fig. 5. Mass transport coefficient and diffusion coefficient as functions of $\left(\frac{1}{M_{O_2}}+\frac{1}{M_{Diluent}}\right)^{1/2}$ (a), $\frac{1}{\sigma_{O_2-Diluent}}$ (b), and $\sqrt{\left(\frac{1}{M_A}+\frac{1}{M_B}\right)\frac{1}{\sigma_{AB}\Omega_{D,AB}}}$ (c). Experimental diffusion coefficients measured at 60°C were chosen for the plot. For SF_6, the point recorded at 20°C was taken. Theoretical diffusion coefficient values were used for Ne, Kr, and CF_4.

However, Eq. (7) implies that the use of different gas diluents only affects k_g and not k_e. An extrapolation to a zero diluent weight gives the O_2 mass transport coefficient in the electrolyte phase (k_e), which is equal to 0.01284 m s^{-1}. The Fig. 4 inset shows the results only for inert gases diluents because they are monoatomic gases and it is possible to eliminate the impact of the effective molecular diameter. Using only the results of the inert gases gives k_e equals to 0.01391 m s^{-1}, which is relatively close to 0.01284 m s^{-1}. Applying k_e as 0.01284 m s^{-1} and using Eq. (8), k_g in N_2 diluent is equal to 0.02727 m s^{-1}.

4.3. Effect of the O_2 concentration

Fig. 6 a) shows the limiting current density profiles recorded at different oxygen concentration in a mixture with He for the same MEA1. An increase of the oxygen concentration obviously leads to a growth of the limiting current densities of the inlet segments as well as the total cell for all diluents: He, Ne, N_2, Ar, and CO_2. However, segment 1 did not reach the limiting current at 10% O_2, which might impact the mass transport coefficient calculation. Note that under the conditions of a high oxygen concentration in He, the effects of oxygen self-diffusion appears to start playing a significant role, which resulted in a decrease of the mass transport coefficient (Table 5 and Fig. 6 b). A comparison of the data reveals that a high oxygen concentration is not favorable for the mass transport coefficient determination and that it should be not higher than 7% for the method to be effective. Additionally, it should be emphasized that the mass transport coefficient in ionomer phase (k_e) appears to depend on the O_2 concentration in the gas stream, which was unexpected for us. Table 5 presents a ratio between k_e and $k_{g,\ N2}$. There is a decrease in the ratio with an increase of O_2 concentration. Such a dependence most likely results in a different value of the coefficient at real operating conditions, where the O_2 concentration is 21%. This observation should be taken into account for future development of the method.

Table 5. Overall oxygen mass transport coefficients measured at different O_2 concentration. The oxygen mass transport coefficients in the ionomer phase and in N_2 media are also presented. For the case of 5% O_2, k_e and k_g were calculated based on a linear fit for points He to CO_2.

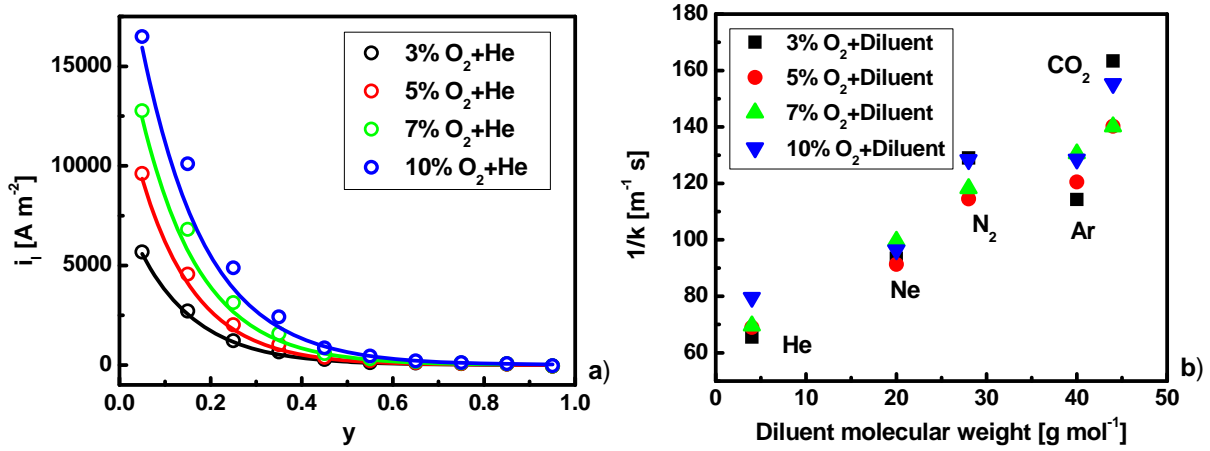| Diluent	M [g mol^{-1}]	k [m s^{-1}]			
		3% O_2	5% O_2	7% O_2	10% O_2
He	4.003	0.01524	0.0145	0.01437	0.01257
Ne	20.183	0.0107	0.01096	0.01004	0.01037
N_2	28.01	0.00775	0.00873	0.00846	0.00779
Ar	39.948	0.00875	0.0083	0.00766	0.00778
CO_2	44.01	0.00612	0.00713	0.00714	0.00644
k_e [m s^{-1}]		0.01735	0.01622	0.01545	0.01429
$k_{g,\ N2}$ [m s^{-1}]		0.01401	0.01890	0.01870	0.01713
$k_e/k_{g,\ N2}$		1.238	0.858	0.826	0.834

Fig. 6. Limiting current density profiles at different O_2 content in He (a). Effect of the diluent molecular weight on the overall oxygen mass transport coefficient at different O_2 concentrations (b).

4.4. **Effect of temperature**

Diffusion is a temperature-activated process that results in a higher mass transport coefficient with a higher temperature. The effects of temperature on the oxygen mass transport coefficient were studied from 40 to 80°C and for the diluents of He, Ne, N_2, Ar, and CO_2. Fig. 7 a) and Table 6 show the overall oxygen mass transport coefficient as function of diluent molecular weight at different temperatures. These results allow the oxygen mass transport coefficients in ionomer and gas phases to be calculated (Table 7). A dependence of the ionomer and the gas phase mass transfer coefficients on temperature is presented on Fig. 7 b). The mass transport coefficient in gas phase was found to increase with operating temperature for all diluents (Ne, N_2, Ar, and CO_2). It should be noted Knudsen diffusion increases as $T^{1/2}$ (Eq. 15), whereas bulk diffusion varies as $T^{3/2}$ (Eq. 9) [4]. However, based on our data, it is difficult to distinguish which type of diffusion we observed, but most likely, both diffusion processes occurred.

The behavior of the mass transport coefficient in the ionomer phase is more complicated. It is possible to distinguish two regions: an increase of the coefficient at 40-60°C and a decrease of the coefficient at 70-80°C. The calculated k_e values vs. inverse of the temperature (Arrhenius plot) are shown in Fig. 7 c). Empirically, the following equation can be adopted to describe the temperature dependence of the oxygen mass transport through the ionomer phase:

$$k_e = \frac{D_e}{\delta} = \frac{D_o}{\delta} e^{-\frac{E_a}{RT}} \qquad\qquad (16)$$

where E_a is the activation energy, T is the cell temperature, and D_o is a constant independent of temperature. One would expect a linear relationship between lnk_e and $1/T$, which would enable the activation energy to be determined from the slope [31-37]. However, in our case, we should exclude the points at 70 and 80°C from a linear fit. The other points exhibit a linear trend, with a slope corresponding to the activation energy of 10.6 kJ mol^{-1}. The obtained value is smaller in comparison with what was reported for Nafion membranes previously: 5.5 kcal mol^{-1} (or 23 kJ mol^{-1}) [31, 36]; 5.7±0.2 kcal mol^{-1} (or 23.8±0.8 kJ mol^{-1}) [32]; 20.47 kJ mol^{-1} [37].

The decrease of k_e and a deviation from the Arrhenius law at 70°C and 80°C can be explained by measurements under real fuel cell operating conditions and the possible excessive water production, which might lead to water condensation and oxygen diffusion not only through the ionomer but also through the liquid phase [5]. Although the ionomer mass transport coefficient increases with temperature, the existence of the liquid film may create an additional barrier for O_2 diffusion, which may lead to a decrease of the apparent O_2 k_e.
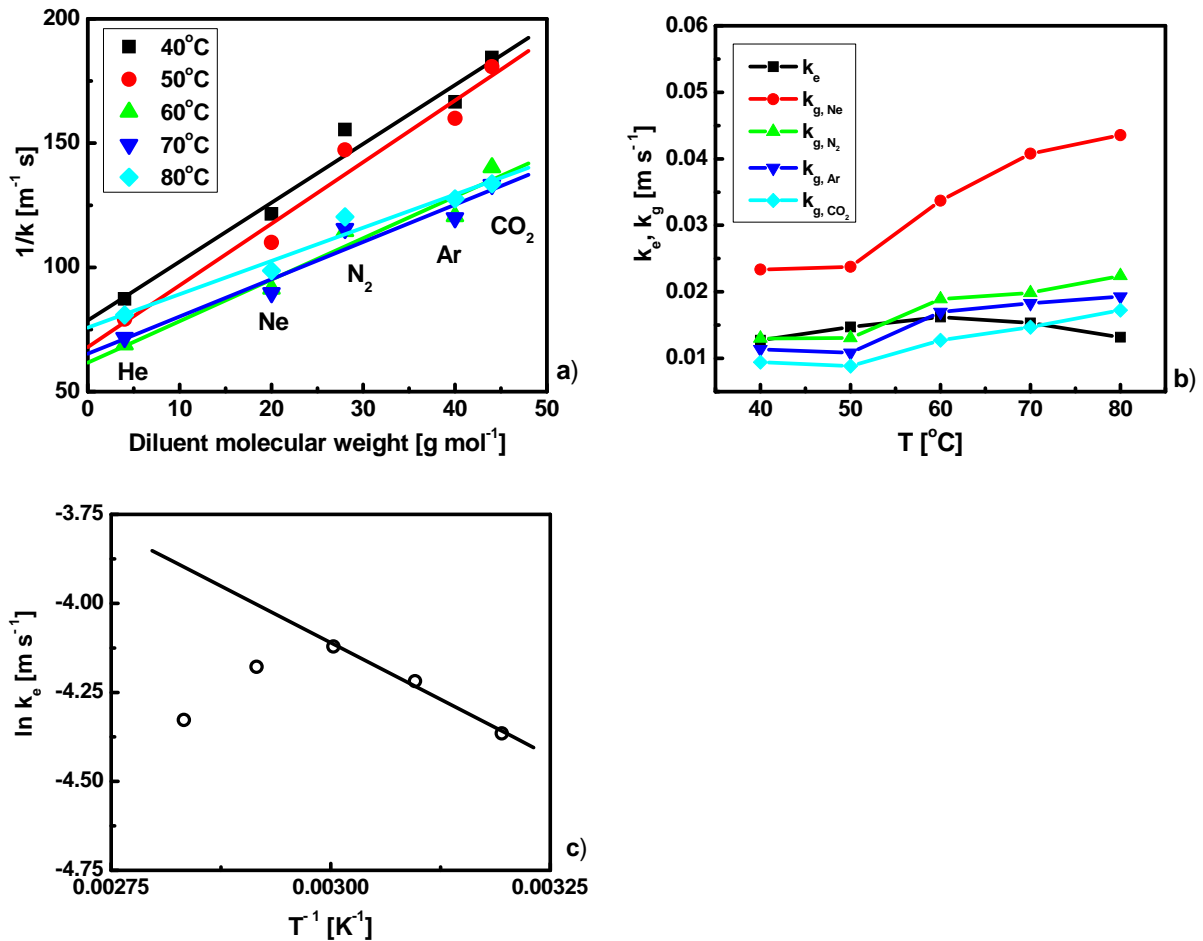

Fig. 7. Effect of the diluent molecular weight on the overall oxygen mass transport coefficient at different temperatures (a). Temperature dependence of the ionomer and gas phase coefficients (b). Arrhenius plot of k_e (c).

Table 6. Overall oxygen mass transport coefficients measured at different temperatures.

Diluent	M [g mol^{-1}]	k [m s^{-1}]				
		40°C	50°C	60°C	70°C	80°C
He	4.003	0.01145	0.01263	0.0145	0.01394	0.01237
Ne	20.183	0.00823	0.00909	0.01095	0.01114	0.01013
N_2	28.01	0.00643	0.00692	0.00873	0.00865	0.00831
Ar	39.948	0.006	0.00625	0.0083	0.00834	0.007835
CO_2	44.01	0.00542	0.00553	0.00713	0.0075	0.00748

Table 7. Oxygen mass transport coefficients in the ionomer and gaseous phases. For the case of 60°C, k_e and k_g were calculated based on a linear fit for points He to CO_2.

	40°C	50°C	60°C	70°C	80°C
k_e [m s^{-1}]	0.01271	0.01472	0.01622	0.01533	0.0132
$k_{g, Ne}$ [m s^{-1}]	0.02335	0.02377	0.03370	0.04076	0.04356
$k_{g, N2}$ [m s^{-1}]	0.01301	0.01306	0.01891	0.01985	0.02243
$k_{g, Ar}$ [m s^{-1}]	0.01137	0.01086	0.01699	0.01829	0.01928
$k_{g, CO2}$ [m s^{-1}]	0.00945	0.00886	0.01272	0.01468	0.01726

4.5. Effect of cathode Pt loading

MEA1 and MEA2 were used for evaluation of the impact of cathode Pt loading on the O_2 mass transport coefficient. Table 8 lists the overall ECA anode and cathode for both samples, and Fig. 8 presents the anode and cathode ECA distributions. As expected, the anode ECA for both samples is close, while the cathode ECA differs by a factor of two. An increase of the cathode Pt loading resulted in a performance growth of the individual segments as well as of the overall cell. The polarization curves for segments 1, 4, 7, and 10 are plotted in Fig. 9. The results of these four segments were representative of the trends observed in the entire cell. The observed performance of MEA2 is higher than that of MEA1. Analysis of the performance losses [12] demonstrated that the improved MEA2 performance results from a decreased activation and mass transport overpotentials in comparison with MEA1. The observed decrease of these overpotentials can account for a higher ECA and improved water management within the GDL due to a slightly higher compression ratio.

Table 8. Anode and cathode ECA for MAE1 and MEA2.

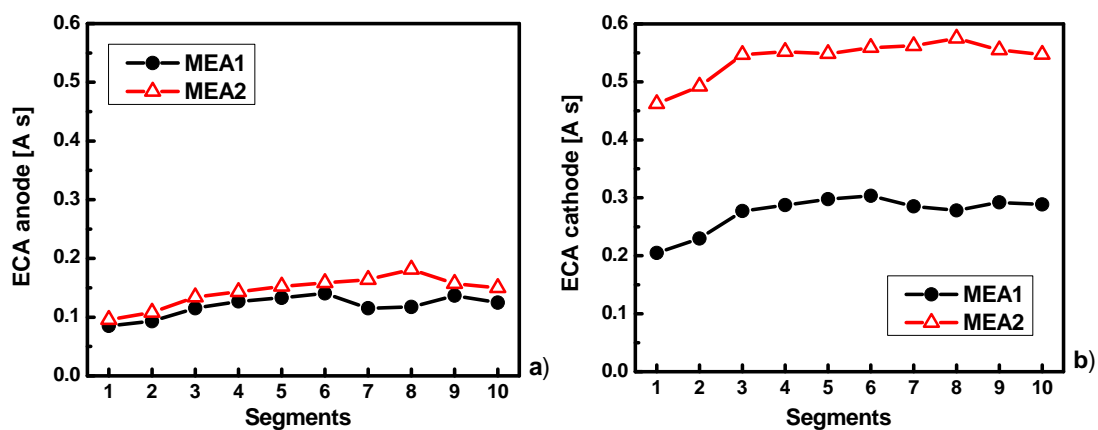| Sample	An/Ca Pt loading [mg cm^{-2}]	Anode ECA [A s]	Cathode ECA [A s]
MEA1	0.1/0.2	1.188	2.744
MEA2	0.1/0.4	1.445	5.401

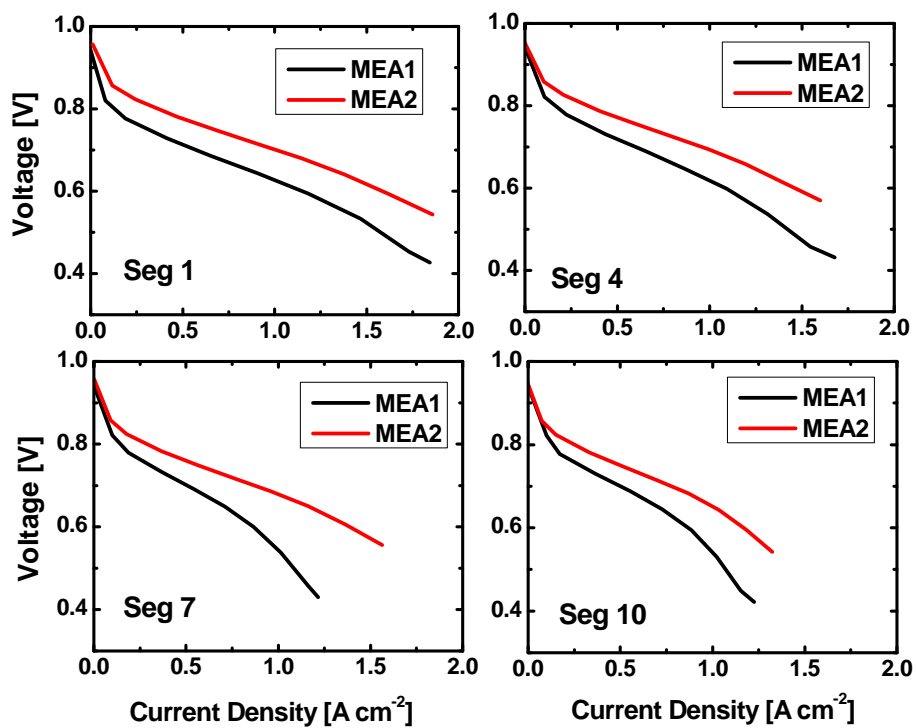Fig. 8. ECA anode (a) and cathode (b) distributions for MEA1 and MEA2.

Fig. 9. Polarization curves for segments 1, 4, 7, and 10 for MEA1 and MEA2 samples. Anode/cathode: H_2/air, 2/2 stoichiometry, 100/50% RH, 48.3/48.3 kPa_g, 60°C.
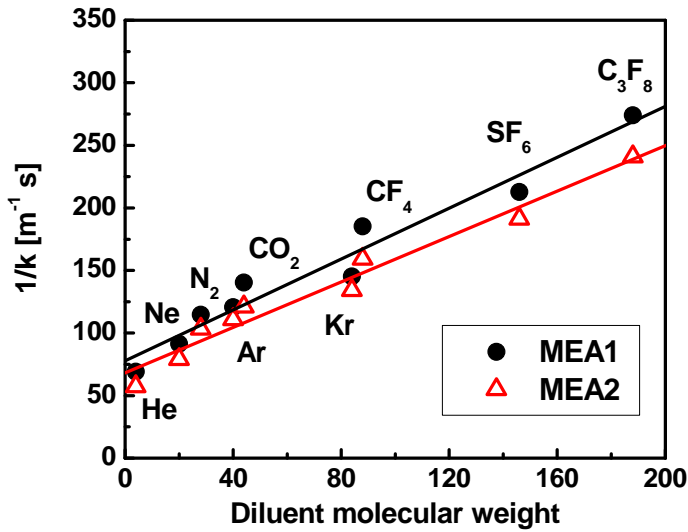
Fig. 10. Effect of the diluent molecular weight on the overall oxygen mass transport coefficient for MEA1 and MEA2.

The impact of the diluent molecular weight on the inverse overall mass transport coefficient for MEA1 and MEA2 is shown in Fig. 10. A linear relationship was observed for both MEA2 and MEA1, which gave us an opportunity to extract the oxygen mass transport coefficient in both the ionomer and gas phases. Taking into account all the diluent points, the mass transport coefficient in ionomer (k_e) is 0.01465 m s^{-1} for MEA2, whereas for MEA1 it is 0.01284 m s^{-1}. Despite the factor of 2 increased in both the Pt loading and the ECA, the variation in the ionomer mass transport coefficients is not so significant. The deviation between these two values can be explained by the fact that the MEAs were taken out from two different batches, so a difference in the ionomer coating of the electrode layers is possible. However, the oxygen mass transport coefficient in nitrogen media ($k_{g, N2}$) was found to be very similar: 0.02727 and 0.02853 m s^{-1} for MEA1 and MEA2, respectively, as expected.

4.6. Effect of GDL

To study the effect of the GDL on the oxygen mass transport coefficient, two different diffusion media by Sigracet were examined: 25BC and 25BA. Table 9 shows the main parameters of these GDLs. 25BA has the same carbon paper substrate, but does not have a microporous layer (MPL), which is accompanied by a variation of the GDL thickness, air permeability, area weight, and even porosity. Tests were performed with two MEA samples: MEA2 and MEA3, which have the same Pt loading and belong to the same MEA batch. Table 10 presents the overall anode and cathode ECAs for these samples, and Fig. 11 shows the ECA distribution as a function of a segment position downstream. The overall ECA as well as the individual segment ECA were found to be close for these both samples.

26

In spite of the similar anode and cathode ECA, the performance of MEA3 is lower than performance of MEA2 at high current density, due to the different properties of the GDLs used (Fig. 12). MPL was shown to provide better electrical contact and mechanical compatibility between the layers. Additionally, MPL reduces the cathode GDL flooding because it alters the liquid water distribution in the cell to a more favorable arrangement for gas phase transport [38-44]. The lack of MPL in the GDL results in a decrease of the fuel cell performance, due to an increase of high frequency resistance (HFR) and poor water management. Analysis of the overpotentials [12] indicates that the performance loss occurs mainly due to an increase of the mass transport and the ohmic losses for MEA3. HFR of individual segments varies in the range from $0.063\ \Omega\ cm^2$ to $0.073\ \Omega\ cm^2$ for MEA2; in the case of MEA3, the HFR is $0.070\text{-}0.093\ \Omega\ cm^2$, which leads to an increase of the ohmic overpotential for the MEA3.

Table 9. Manufacturer specifications of the GDL materials used.

GDL	Thickness [μm]	Area weight [g m^{-2}]	Porosity [%]	Air permeability [cm^3 cm^{-2} s^{-1}]	Resistance [mΩ cm^2]	MPL	PTFE [%]
25BA	185[a]	40	88	210[b]	<10[c]	No	5
25BC	235[a]	86	80	1[b]	<12[c]	Yes	5

[a] – measured at 0.25 N cm^{-2}; [b] – Gurley model 4118, 300 cm^3, 0.645 cm^2 in orifice; [c] – through plane, 2-point measurement, circular (25 mm) gold-plated contacts at pressure of 10 bar.

Table 10. Anode and cathode ECA for MAE2 and MEA3.

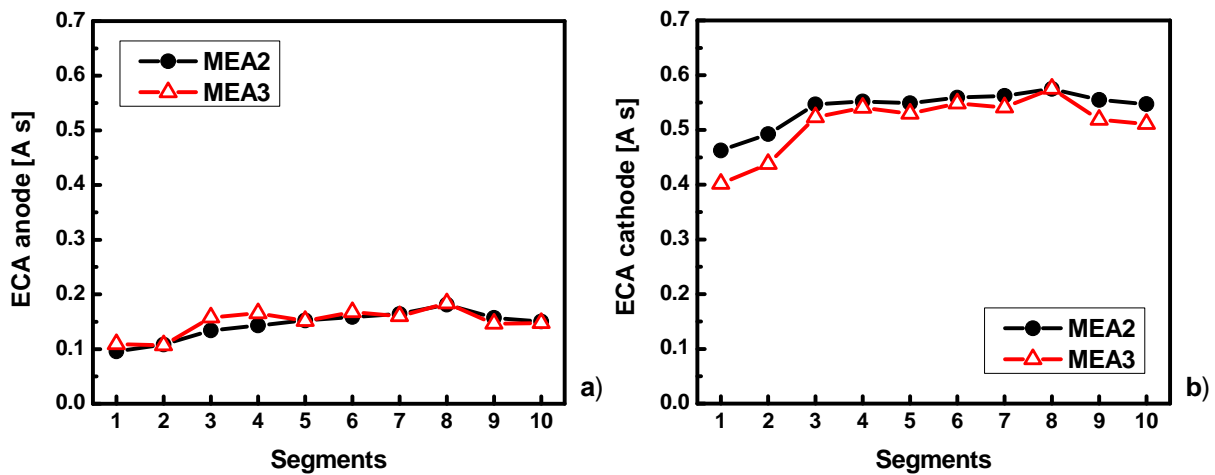| Sample	An/Ca Pt loading [mg cm^{-2}]	Anode ECA [A s]	Cathode ECA [A s]
MEA2	0.1/0.4	1.445	5.401
MEA3	0.1/0.4	1.497	5.129

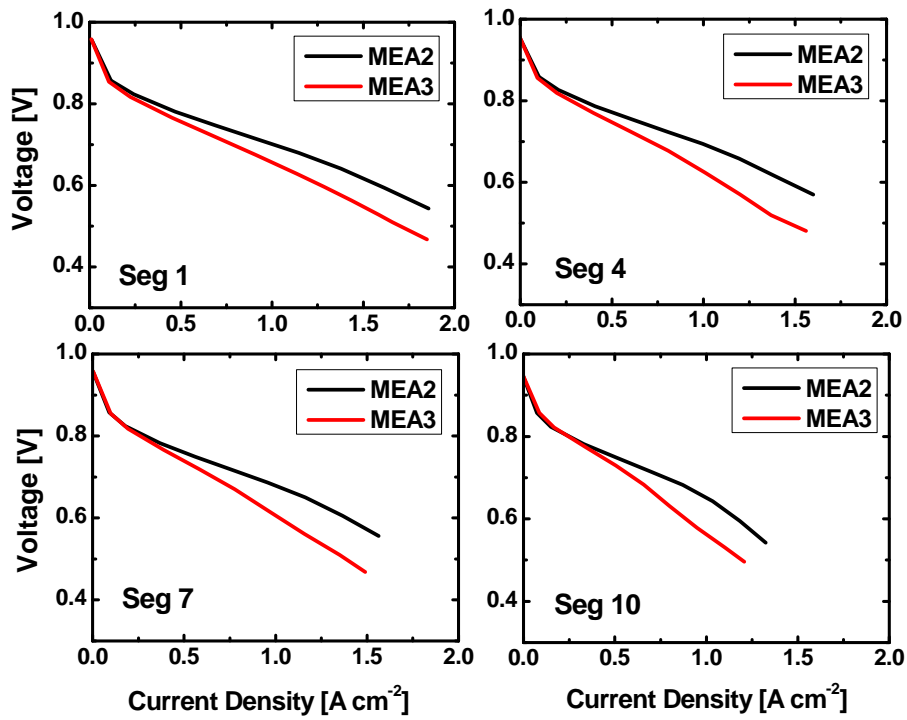Fig. 11. ECA anode (a) and cathode (b) distributions for MEA2 and MEA3.

Fig. 12. Polarization curves for segments 1, 4, 7, and 10 for MEA2 and MEA3 samples. Anode/cathode: H_2/air, 2/2 stoichiometry, 100/50% RH, 48.3/48.3 kPa_g, 60°C.
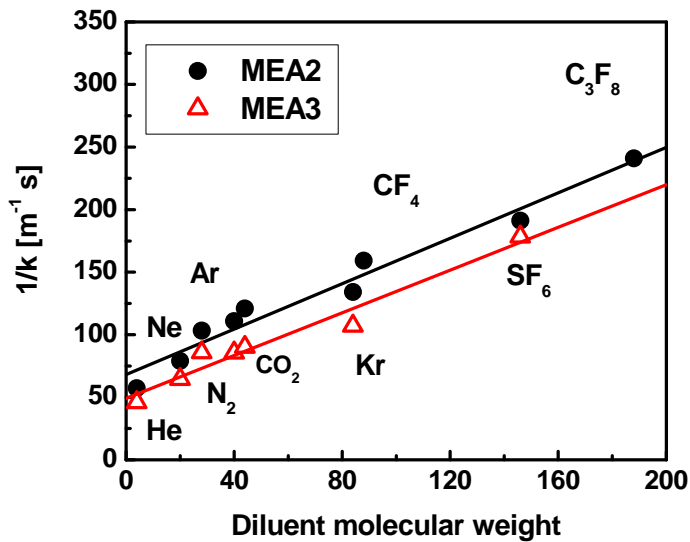

Fig. 13. Effect of the diluent molecular weight on the overall oxygen mass transport coefficient for MEA2 and MEA3.

The dependence of the inverse overall mass transport coefficient vs. the diluent molecular weight for MEA2 and MEA3 is presented in Fig. 13. There was not enough CF_4 and C_3F_8 for performing VI measurements for MEA3; thus, the plot does not present these data. A linear relationship was observed for MEA3 as well as for MEA1 and 2, which enables the extraction of the oxygen mass transport coefficient in the ionomer and gas phases. Taking into account all the diluent points, the mass transport coefficient in the ionomer (k_e) is 0.02032 m s^{-1} for MEA3, whereas for MEA2 it is 0.01465 m s^{-1}. The oxygen mass transport coefficient in nitrogen media ($k_{g,\,N2}$) was found to be very similar: 0.02853 and 0.02736 m s^{-1} for MEA2 and MEA3, respectively.
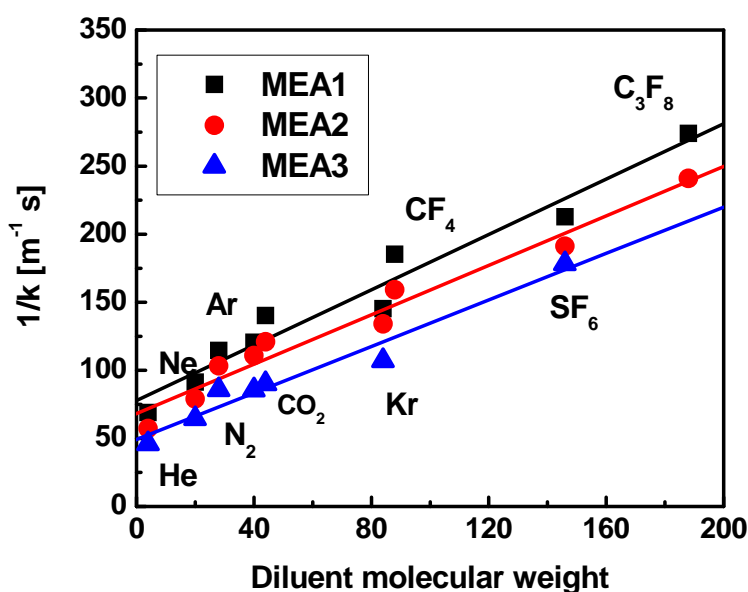

Fig. 14. Effect of the diluent molecular weight on the overall oxygen mass transport coefficient for MEA1, MEA2 and MEA3.

The observed difference between the oxygen mass transport coefficients for MEA2 and MEA3 partially may be attributed to the deviations in the ionomer content on the Pt layer; however, a lack of MPL for MEA3 GDL might make its own contribution to oxygen transport in the GDE. The MPL consists of carbon or graphite particles mixed with a polymeric binder, usually PTFE. The thickness of the MPL is ~ 50 μm for 25BC, which is greater than the cathode catalyst layer thickness (~ 20 μm). Additionally, the MPL textural properties are very similar to the catalyst layer texture: close values of porosity and pore size. For example, the pore size distribution data for the GDL with MPL revealed pores with sizes in the range of 20-100 nm in the MPL [45, 46]. Taking into account the pore size of the MPL, we could assume that both Knudsen and bulk diffusion could occur in the MPL and that both most likely contribute to the ionomer term. The proposed method for separating the oxygen mass transport coefficient in the ionomer and gas phases most likely presents the ionomer contribution as a sum of diffusion processes in the ionomer and MPL.

To verify this hypothesis, it seems reasonable to study the impact of MPL on the mass transport coefficient in the ionomer and gas phases. Variation of the MPL loading will provide the necessary data for further development of the method. Note that this finding might be connected with the results presented in Table 5 because MPL impacts k_e, so it may be responsible for the variation of the mass transport coefficients with the O_2 concentration in the gas stream.

Table 11. The oxygen mass transport coefficients and resistances in the ionomer and gaseous (N_2) phases. The calculations were performed using all the diluents points.

Sample	k_e [m s^{-1}]	$k_{g, N2}$ [m s^{-1}]	R_e [s cm^{-1}]	$R_{g, N2}$ [s cm^{-1}]
MEA1	0.01284	0.02727	0.7788	0.3667
MEA2	0.01465	0.02853	0.6826	0.3505
MEA3	0.02032	0.02736	0.4921	0.3655

Fig. 14 and Table 11 provide summary data about MEAs under the study. The oxygen mass transport coefficient in gas phase was found to be similar for all tested MEAs, however a difference was observed for the O_2 mass transfer coefficient in the ionomer. A variation between MEA1 and MEA2 might be explained by different ionomer coverage in the cathode layer because the samples were from two different batches. At the same time, the lack of a MPL in MEA3 gives a higher value of the oxygen ionomer mass transport coefficient, which allows us to estimate the contribution of the MPL and the catalyst layer (CL) on the oxygen mass transport.

$$\frac{1}{k_{e,MEA2}} = \frac{1}{k_{e,CL,MEA2}} + \frac{1}{k_{e,MPL,MEA2}} \tag{17}$$

$$k_{e,CL,MEA2} = k_{e,CL,MEA3} = k_{e,MEA3} \tag{18}$$

$$k_{e,MPL,MEA2} = \frac{k_{e,MEA3} \cdot k_{e,MEA2}}{k_{e,MEA3} - k_{e,MEA2}} \tag{19}$$

The oxygen mass transfer coefficient within the MPL is $0.0525\ \mathrm{m\ s^{-1}}$, or the mass transport resistance is $0.1905\ \mathrm{s\ cm^{-1}}$. The obtained results from Table 11 suggest that the oxygen mass transfer coefficient in N_2 media accounts for ~32-34% of the overall mass transport processes. The mass transport within the MPL amounts to ~18%. Combining these two terms leads to the conclusion that for transport through the ionomer and water phases, Knudsen diffusion in the catalyst layer accounts for ~48-50% of the overall mass transport coefficient, which is in good agreement with previously reported data [5]. Because the ionomer (including MPL) and gas phase contributions are approximately similar, there is an opportunity to optimize the design by targeting both the GDL and the catalyst layer, which would not have been the case if one contribution was overwhelmingly dominant.

5. Conclusions

1. A method for determination of the oxygen mass transport coefficient using local limiting current distribution was developed.

2. Validation of the new method was performed using a segmented cell system for the measurements of the local limiting current under potentiostatic control of the cell. The obtained mass transport coefficient values were compared with the mass transfer coefficient determined by the available traditional method involving measurement of overall cell limiting current at different reagent flow rates. A comparison demonstrated the validity of the new method.

3. An application of the empirical correlation between overall mass transport coefficient and diluent molecular weight to separate the mass transport contributions in ionomer and gas phases was proposed. A linear relationship between the inverse overall mass transport coefficient and the diluent molecular weight was revealed. Because the different gas diluents used with different molecular weights only affect the mass transport coefficient in the gas phase (Eq. 7), an extrapolation to a zero diluent weight yields the O_2 mass transport coefficient in the ionomer phase, k_e. In a second step, the k_g value is calculated with Eq. (8) using the extrapolated k_e value and the measured k value. k_e was determined to be equal to 0.01284, and $k_{g,\,N2}$ was equal to 0.02727 m s^{-1}. The method was successfully applied, and a comparison of the obtained results with the literature data demonstrated the validity of the approach.

4. The effects of some of the operating conditions on the mass transport coefficient were studied.
4.1. A high O_2 concentration (up to 10%) in the cathode gas stream affects the determination of the mass transfer coefficient because the inlet segments do not reach the limiting current under this condition. The O_2 concentration should be in the range 3-5% for the proposed method to be effective.
4.2. The effect of operating temperature on the ionomer and gas phases mass transport coefficients was studied at 40-80°C. The mass transport coefficient in the gas phase was found to increase with temperature. An increase of the ionomer mass transport coefficient was found over the range of 40-60°C, and its decrease was observed over the range of 70-80°C. The finding might be related to excessive water production and its condensation at these temperatures, resulting in oxygen diffusion through the liquid phase, which affects the temperature dependence of the ionomer mass transfer coefficient.

5. Application of the method for characterization of MEAs with different cathode Pt loading and GDL revealed the following:
5.1. The variation of Pt loading does not significantly change $k_{g,N2}$; however, a slight increase of k_e was detected, most likely due to ionomer coverage variations of the catalyst layer for MEAs from different batches.
5.2. The application of the GDL without MPL also does not change $k_{g,N2}$, but results in an increase of $k_{e,}$ which is assumed to be related to the MPL impact on the determination of the ionomer contribution of the mass transport coefficient.

6. Future work

- Extend the method and mathematical model to lower current densities (is there an effect of current density on the mass transfer coefficient that is measured?).
- Simplify the method by decreasing the number of diluents required (is the analysis error impacted by using fewer diluents?).
- Study the effects of several operating conditions (relative humidity and back pressure).
- Evaluate the MPL impact on the ionomer mass transport coefficient for further method development.
- Repeat some experiments with the different MEAs from the same batch for a better understanding of the variability and to ensure reproducibility of the method.
- Cross-validate the method with an impedance spectroscopy approach developed at ANL in collaboration with Nuvera and others (are the mass transfer coefficients reliable?).
- Test the applicability of the method to other catalyst layer structures, such as the 3 M nano-structured thin films (in absence of Nafion, does the method still provide a reliable gas phase mass transfer coefficient?).
- Extend the method to study the hydrogen mass transfer coefficient and its applicability to other fuel cell types (alkaline fuel cell).

7. Bibliography

[1] T. J. Gross, A. J. Poche Jr., K. C. Ennis, *Beyond Demonstration: the Role of Fuel Cells in DoD's Energy Strategy*, LMI, McLean, VA (2011).

[2] A.A. Kulikovsky, Electrochem. Commun. 4 (2002) 845.

[3] M. V. Williams, E. Begg, L. Bonville, H. R. Kunz, and J. M. Fenton, J. Electrochem. Soc. 151 (2004) A1173.

[4] S. S. Kocha, in *Handbook of Fuel Cells: Fundamentals, Technology and Applications*, Vol. 3, W. Vielstich, A. Lamm, and H. A. Gasteiger, Editors, p. 538, John Wiley & Sons, New York (2003).

[5] U. Beuscher, J. Electrochem. Soc. 153 (2006) A1788.

[6] D. R. Baker, D. A. Caulk, K. C. Neyerlin, and M. W. Murphy, J. Electrochem. Soc. 156 (2009) B991.

[7] D.A. Caulk, D.R. Baker, J. Electrochem. Soc. 157 (2010) B1237.

[8] D.A. Caulk, D.R. Baker, ECS Trans. 50 (2) (2012) 35.

[9] J. Stumper, H. Haas, A. Granados, J. Electrochem. Soc. 152 (2005) A837.

[10] J. St-Pierre, B. Wetton, G.-S. Kim, and K. Promislow, J. Electrochem. Soc. 154 (2007) B186.

[11] J. St-Pierre, Fuel Cells 11 (2011) 263.

[12] T. V. Reshetenko, G. Bender, K. Bethune, R. Rocheleau, Electrochim. Acta, 56 (2011) 8700.

[13] S. J. C. Cleghorn, C. R. Derouin, M. S. Wilson, S. Gottesfeld, J. Appl. Electrochem., 28 (1998) 663.

[14] J. Stumper, S. A. Campbell, D. P. Wilkinson, M. C. Johnson, M. Davis, Electrochim. Acta, 43 (1998) 3773

[15] C. Wieser, A. Helmbold, E. Gülzow, J. Appl. Electrochem., 30 (2000) 803.

[16] G. Bender, M. S. Wilson, T. A. Zawodzinski, J. Power Sources, 123 (2003) 163.

[17] T.R. Ralph, M.P. Hogarth, Platinum Metals Rev. 46 (2002) 3.

[18] R. B. Bird, W. E. Stewart, E. N. Lightfoot, *Transport Phenomena*, revised 2nd edition, John Wiley & Sons, New York, 2007, pp. 687-690.

[19] Z. Liu, L. Yang, Z. Mao, W. Zhuge, Y. Zhang, L. Wang, J. Power Sources, 157 (2006) 166.

[20] P. Berg, K. Promislow, J. St-Pierre, J. Stumper, B. Wetton, J. Electrochem. Soc. 151 (2004) A341.

[21] Y.W. Rho, O.A. Velev, S. Srinivasan, Y.T. Kho, J. Electrochem. Soc. 141 (1994) 2084.

[22] R.B. Bird, W.E. Stewart, E.N. Lightfoot, "Transport phenomena", 2[d] edition, John Wiley and Sons, New York, 2002, pp. 513-542.

[23] A. Weber, R.Darling, J. Meyers, J. Newman, in *Handbook of Fuel Cells: Fundamentals, Technology and Applications*, Vol. 1, W. Vielstich, A. Lamm, and H. A. Gasteiger, Editors, pp. 45-70 , John Wiley & Sons, New York (2003).

[24] E.B. Winn, Phys. Rev. 80 (1950) 1024

[25] Spravochnik khimika (Chemistry handbook, in Russian), Vol. 3, Ed. B.P. Nikolskii, 2[d] edition, Moscow, 1965, pp. 906-920.

[26] D.R. Lide, "Handbook of chemistry and physics" 89 edition 2008-2009, CRC Press, pp. 6-213-214.

[27] S.L. Seager, L.R. Geertson, J.C. Giddings, J. Chem. Eng. Data 8 (1963) 168.

[28] http://compost.css.cornell.edu/oxygen/oxygen.diff.air.html

[29] http://chemanalytica.com/book/novyy_spravochnik_khimika_i_tekhnologa/08_elektrodnye_protsessy_khimicheskaya_kinetika_i_diffuziya_kolloidnaya_khimiya/5017 (Russian).

[30] Spravochnik khimika (Chemistry handbook, in Russian), Vol. 1, Ed. B.P. Nikolskii, Moscow, 1966, pp. 389-390.

[31] Z. Ogumi, Z. Takehara, S. Yoshizawa, J. Electrochem. Soc. 131 (1984) 769.

[32] A. Parthasarathy, S. Srinivasan, A.J. Appleby, J. Electrochem. Soc. 139 (1992) 250.

[33] R.S. Yeo, J. McBreen, J. Electrochem. Soc. 126 (1979) 1682

[34] T. Sakai, H. Takenaka, N. Wakabayashi, Y. Kawami, E. Torikai, J. Electrochem. Soc. 132 (1985) 1328.

[35] K. Broka, P. Ekdunge, J. Appl. Electrochem. 27 (1997) 117.

[36] J. Zhang, H.A. Gasteiger, W. Gu, J. Electrochem. Soc. 160 (2013) F616.

[37] C.K. Mittelsteadt, H. Liu, in *Handbook of Fuel Cells: Fundamentals, Technology and Applications*, Vol. 5, chapter 22, W. Vielstich, A. Lamm, and H. Yokokawa, Editors, p. 345, John Wiley & Sons, New York (2009).

[38] L. Cindrella, A.M. Kannan, J.F. Lin, K. Saminathan, Y. Ho, C.W. Lin, J. Wertz, 194 (2009) 146.

[39] A.Z. Weber, J. Newman, J. Electrochem. Soc. 152 (2005) A677.

[40] J.T. Gostick, M.A. Ioannidis, M.W. Fowler, M.D. Pritzker, Electrochem. Com. 11 (2009) 576.

[41] Z. Qi, A. Kaufman, J. Power Sources 109 (2002) 38.

[42] J.H. Nam, M. Kaviany, Int. J. Heat Mass Trans 46 (2003) 4595.

[43] U. Pasaogullari, C.Y. Wang, J. Electrochem. Soc. 151 (2004) A399.

[44] T.V. Reshetenko, G. Bender, K. Bethune, R. Rocheleau, Electrochim. Acta 80 (2012) 368-376.

[45] S. Park, J.-W. Lee, B.N. Popov, J. Power Sources 163 (2006) 357.

[46] M.F. Mathias, J. Roth, J. Fleming, W. Lehnert, in *Handbook of Fuel Cells: Fundamentals, Technology and Applications*, Vol. 3, W. Vielstich, A. Lamm, and H. A. Gasteiger, Editors, pp. 517-537, John Wiley & Sons, New York (2003).